Formation of Hard Power Laws in the Energetic Particle Spectra Resulting from Relativistic Magnetic Reconnection

Fan Guo, Hui Li, William Daughton, and Yi-Hsin Liu
Los Alamos National Laboratory, P.O. Box 1663, Los Alamos, New Mexico 87545, USA
(Received 15 May 2014; published 8 October 2014)

Using fully kinetic simulations, we demonstrate that magnetic reconnection in relativistic plasmas is highly efficient at accelerating particles through a first-order Fermi process resulting from the curvature drift of particles in the direction of the electric field induced by the relativistic flows. This mechanism gives rise to the formation of hard power-law spectra in parameter regimes where the energy density in the reconnecting field exceeds the rest mass energy density $\sigma \equiv B^2/(4\pi n m_e c^2) > 1$ and when the system size is sufficiently large. In the limit $\sigma \gg 1$, the spectral index approaches $p = 1$ and most of the available energy is converted into nonthermal particles. A simple analytic model is proposed which explains these key features and predicts a general condition under which hard power-law spectra will be generated from magnetic reconnection.

DOI: 10.1103/PhysRevLett.113.155005 PACS numbers: 52.27.Ny, 52.35.Vd, 98.54.Cm, 98.70.Rz

Introduction.—Magnetic reconnection is a fundamental plasma process that allows rapid changes of magnetic field topology and the conversion of magnetic energy into plasma kinetic energy. It has been discussed extensively in solar flares, Earth's magnetosphere, and laboratory applications. However, magnetic reconnection remains poorly understood in high-energy astrophysical systems [1]. Magnetic reconnection has been suggested as a mechanism for producing high-energy emissions from pulsar wind nebula, gamma-ray bursts, and jets from active galactic nuclei [2–6]. In those systems, it is often expected that the magnetization parameter $\sigma \equiv B^2/(4\pi n m c^2)$ exceeds unity. Most previous kinetic studies focused on the nonrelativistic regime $\sigma < 1$ and reported several acceleration mechanisms, such as acceleration at X-line regions [7–9] and Fermi-type acceleration within magnetic islands [8–11]. More recently, the regime $\sigma = 1$–100 has been explored using pressure-balanced current sheets, and strong particle acceleration has been found in both diffusion regions [12–15] and island regions [16,17]. However, this initial condition requires a hot plasma component inside the current sheet to maintain force balance, which may not be justified for high-σ plasmas.

For magnetically dominated systems, it has been shown [18,19] that the gradual evolution of the magnetic field can lead to formation of intense nearly force-free current layers where magnetic reconnection may be triggered. In this Letter, we perform large-scale two-dimensional (2D) and three-dimensional (3D) full particle-in-cell (PIC) simulations of a relativistic force-free current sheet with σ up to 1600. In the high-σ regime, the release of magnetic energy is accompanied by the energization of nonthermal particles on the same fast time scale as the reconnection process. Much of the magnetic energy is converted into the kinetic energy of nonthermal relativistic particles and the eventual energy spectra show a power law $f(\gamma) \propto \gamma^{-p}$ over nearly two decades, with the spectral index p decreasing with σ and system size and approaching $p = 1$. The dominant acceleration mechanism is a first-order Fermi process through the curvature drift motion of particles along the electric field induced by relativistic reconnection outflows. The formation of the power-law distribution can be described by a simple model that includes both inflow and the Fermi acceleration. This model also appears to explain recent PIC simulations [15], which reported hard power-law distributions after subtracting the initial hot plasma population inside the current layer.

Numerical simulations.—The initial condition is a force-free current layer with $\mathbf{B} = B_0 \tanh(z/\lambda)\hat{x} + B_0 \mathrm{sech}(z/\lambda)\hat{y}$, which corresponds to a magnetic field with magnitude B_0 rotating by 180° across the layer with a thickness of 2λ. The plasma consists of electron-positron pairs with mass ratio $m_i/m_e = 1$. The initial distributions are Maxwellian, with a uniform density n_0 and temperature ($T_i = T_e = 0.36 m_e c^2$). Particles in the sheet have a net drift $\mathbf{U}_i = -\mathbf{U}_e$ to give a current density $\mathbf{J} = e n_0(\mathbf{U}_i - \mathbf{U}_e)$ consistent with $\nabla \times \mathbf{B} = 4\pi \mathbf{J}/c$. The simulations are performed using the VPIC [20] and NPIC codes [21,22], both of which solve the relativistic Vlasov-Maxwell system of equations.

In the simulations, σ is adjusted by changing the ratio of the electron gyrofrequency to plasma frequency $\sigma = B^2/(4\pi n_e m_e c^2) = (\Omega_{ce}/\omega_{pe})^2$. A series of 2D simulations were performed with $\sigma = 1 \rightarrow 1600$ and domain sizes $L_x \times L_z = 300 d_i \times 194 d_i$, $600 d_i \times 388 d_i$, and $1200 d_i \times 776 d_i$, where $d_i = c/\omega_{pe}$ is the inertial length. For 3D simulations, the largest case is $L_x \times L_y \times L_z = 300 d_i \times 300 d_i \times 194 d_i$, with $\sigma = 100$. For high-σ cases, we choose grid sizes $\Delta x = \Delta y = 1.46/\sqrt{\sigma} d_i$ and $\Delta z = 0.95/\sqrt{\sigma} d_i$ so that the gyroradius $\sim v_{\mathrm{the}} d_i/(\sqrt{\sigma} c)$ is resolved. The half thickness is $\lambda = 6 d_i$ for $\sigma \leq 100$, $12 d_i$

for $\sigma = 400$, and $24d_i$ for $\sigma = 1600$ in order to satisfy $U_i < c$. All simulations used more than 100 particles per cell for each species, employed periodic boundary conditions in the x and y directions, and in the z direction used conducting boundaries for the fields and reflecting for the particles. A long-wavelength perturbation [22] with $B_z = 0.03B_0$ is included to initiate reconnection.

Simulation results.—Figure 1 contrasts some key results from 2D and 3D simulations with $\sigma = 100$ and domain size $L_x \times L_z = 300d_i \times 194d_i$. ($L_y = 300d_i$ for the 3D simulation.) Panel (a) shows the current density at $\omega_{pe}t = 375$ in the 2D simulation. Because of the secondary tearing instability, several fast-moving secondary plasmoids develop along the central region and merge to form larger plasmoids [22]. Panel (b) shows an isosurface of current density colored by $\mathbf{J}\cdot\mathbf{E}$ at $\omega_{pe}t = 375$ from the 3D simulation. As the initial guide field is expelled outward from the central region, the kink instability [23] develops and interacts with the tearing mode, leading to a turbulent evolution [24]. Previous studies have suggested different predictions concerning the influence of σ on the reconnection rate [25–29]. In this Letter, the reconnection rate is observed to increase with σ from $E_{\rm rec} \sim 0.03B_0$ for $\sigma = 1$ to $E_{\rm rec} \sim 0.22B_0$ for $\sigma = 1600$. Although the 2D and 3D simulations appear quite different, the energy conversion and particle energization are surprisingly similar. Panel (c) compares the evolution of magnetic energy E_B, plasma kinetic energy E_k, and energy in relativistic particles with $\gamma > 4$. In both cases, about 20% of the magnetic energy is converted into kinetic energy of relativistic particles. Figure 1(d) compares the energy spectra at various times. The most striking feature is that a hard power-law spectrum with index $p \sim 1.35$ forms in both 2D and 3D runs. In the inset, the energy spectrum for all particles in the 3D simulation at $\omega_{pe}t = 700$ is shown by the red line. The low-energy portion can be fitted by a Maxwellian distribution (black line) and the nonthermal part resembles a power-law distribution (blue line) starting at $\gamma \sim 2$, with an exponential cutoff apparent for $\gamma \gtrsim 100$. The nonthermal part contains ~25% of particles and ~95% of the kinetic energy. The maximum particle energy is predicted approximately using the reconnecting electric field $m_e c^2 \gamma_{\rm max} = \int |qE_{\rm rec}| cdt$ until the gyroradius is comparable to the system size. Although we observe a strong kink instability in the 3D simulations, the energy conversion and particle energy spectra are remarkably similar to the 2D results, indicating the 3D effects are not crucial for understanding the particle acceleration. Since there is more freedom to vary the parameters in 2D simulations, in the rest of this Letter we focus on this limit.

In Fig. 2, we present more analysis for the acceleration mechanism using the case with $\sigma = 100$ and $L_x \times L_z = 600d_i \times 388d_i$. Panel (a) shows the energy as a function of the x position of four accelerated particles. The electrons gain energy by bouncing back and forth within the reconnection layer. Upon each cycle, the energy gain is

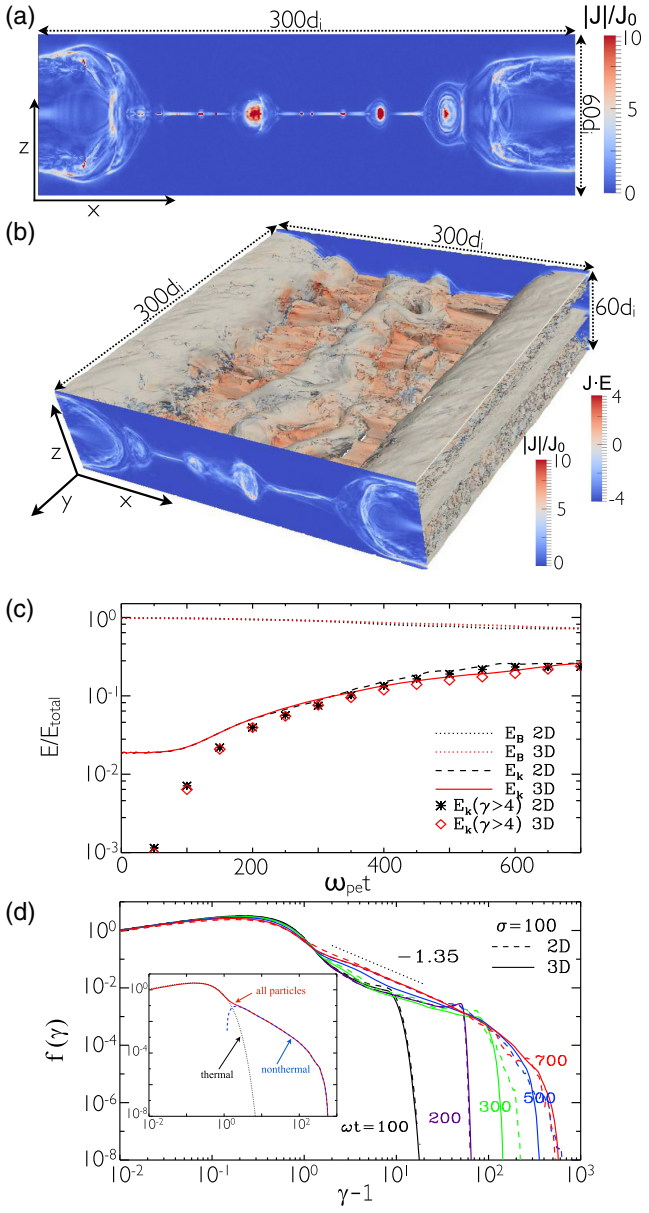

FIG. 1 (color online). Results from 2D and 3D PIC simulations with $\sigma = 100$. (a) Current density from 2D simulation at $\omega_{pe}t = 375$. (b) x-z cut of current density and an isosurface of current density with color-coded $\mathbf{J}\cdot\mathbf{E}$ normalized using $n_0 m_e c^2 \omega_{pe}$ at $\omega_{pe}t = 375$. (c) Evolution of magnetic energy E_B, total kinetic energy E_k, and kinetic energy carried by relativistic particles with $\gamma > 4$. (d) Evolution of particle energy spectra from 2D and 3D simulations. (Inset) Energy spectrum from the 3D simulation at $\omega_{pe}t = 700$.

$\Delta\gamma \sim \gamma$, which demonstrates that the acceleration mechanism is a first-order Fermi process [11,30]. To show this more rigorously, we have tracked the energy change of all the particles in the simulation and contributions from the parallel electric field ($m_e c^2 \Delta\gamma = \int q v_\parallel E_\parallel dt$) and curvature drift acceleration ($m_e c^2 \Delta\gamma = \int q \mathbf{v}_{\rm curv}\cdot\mathbf{E}_\perp dt$) similar to [31], where $\mathbf{v}_{\rm curv} = \gamma v_\parallel^2 (\mathbf{b}\times(\mathbf{b}\cdot\nabla)\mathbf{b})/\Omega_{ce}$, $v_\parallel$ is the particle velocity parallel to the magnetic field, and $\mathbf{b} = \mathbf{B}/|B|$. Panel (b) shows the averaged energy gain and the

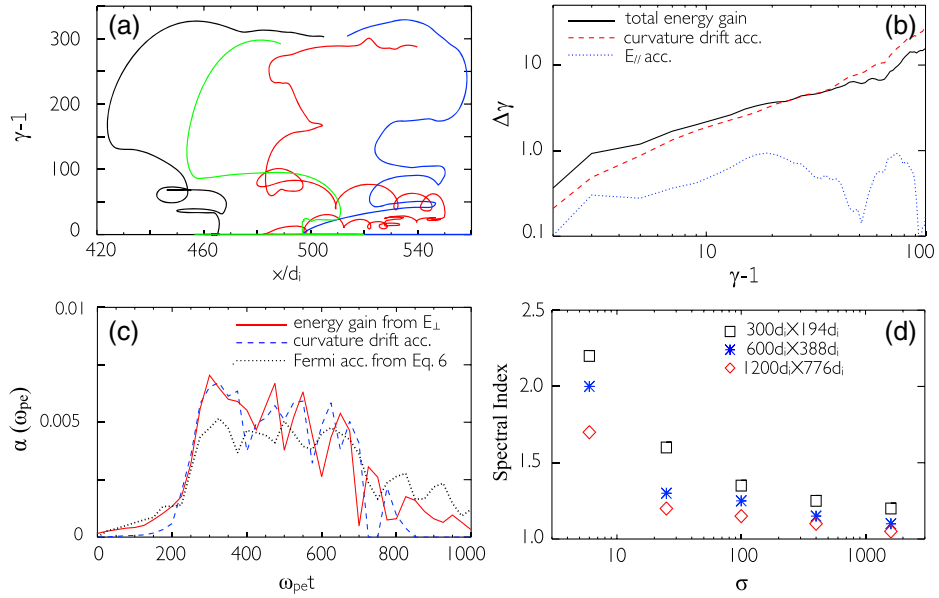

FIG. 2 (color online). (a) Energy as a function of x position of four accelerated particles. (b) Averaged energy gain and contributions from parallel electric fields and curvature drift acceleration over an interval of $25\omega_{pe}^{-1}$ as a function of particle energy starting at $\omega_{pe}t = 350$. (c) $\alpha = \langle\Delta\gamma\rangle/(\gamma\Delta t)$ from energy gain in perpendicular electric field and by curvature drift acceleration, and from Eq. (6) using the averaged flow speed and island size. (d) Spectral index of all 2D simulations.

contribution from parallel electric field and curvature drift acceleration over an interval of $25\omega_{pe}^{-1}$ as a function of energy starting at $\omega_{pe}t = 350$. The energy gain follows $\Delta\gamma \sim \alpha\gamma$, confirming the first-order Fermi process identified from particle trajectories. The energy gain from the parallel motion is weakly dependent on energy, whereas the energy gain from the curvature drift acceleration is roughly proportional to energy. In the early phase, the parallel electric field is strong but accelerates only a small portion of particles, and the curvature drift dominates the acceleration starting at about $\omega_{pe}t = 250$. The contribution from the gradient drift was also evaluated and found to be unimportant. Panel (c) shows $\alpha = \langle\Delta\gamma\rangle/(\gamma\Delta t)$ measured directly from the energy gain of the particles in the perpendicular electric field ($m_e c^2\Delta\gamma = \int q\mathbf{v}_\perp \cdot \mathbf{E}_\perp dt$) and estimated from the expression for the curvature drift acceleration. The close agreement demonstrates that curvature drift term dominates the particle energization. For higher σ and larger domains, the acceleration is stronger and reconnection is sustained over a longer duration. In panel (d), a summary for the observed spectral index of all of the 2D runs shows that the spectrum is harder for higher σ and larger domain sizes, and it approaches the limit $p = 1$.

New Model.—It is often argued that some loss mechanism is needed to form a power-law distribution [12,30]. However, the simulation results reported here illustrate clear power-law distributions in a closed system. Here we demonstrate that these results can be understood in terms of a model illustrated in Fig. 3(a). As reconnection proceeds, the ambient plasma is injected into the acceleration region at a speed $V_{\rm in} = c\mathbf{E}_{\rm rec} \times \mathbf{B}/B^2$. We consider the continuity equation for the energy distribution function $f(\varepsilon, t)$ within the acceleration region

$$\frac{\partial f}{\partial t} + \frac{\partial}{\partial \varepsilon}\left(\frac{\partial \varepsilon}{\partial t} f\right) = \frac{f_{\rm inj}}{\tau_{\rm inj}} - \frac{f}{\tau_{\rm esc}}, \tag{1}$$

with $\partial\varepsilon/\partial t = \alpha\varepsilon$, where α is the constant acceleration rate from the first-order Fermi process, $\varepsilon = m_e c^2(\gamma - 1)/T$ is the normalized kinetic energy, $\tau_{\rm inj}$ is the time scale for injection of particles from the upstream region with fixed distribution $f_{\rm inj}$ and $\tau_{\rm esc}$ is escape time. We assume that the initial distribution within the layer f_0 and the upstream injected distribution are both Maxwellian with initial temperature $T < m_e c^2$, such that

$$\begin{aligned} f_{\rm inj} &\propto \gamma(\gamma^2 - 1)^{1/2}\exp(-\varepsilon) \\ &\approx \sqrt{2\varepsilon}\left(1 + \frac{5T}{4m_e c^2}\varepsilon + \cdots\right)\exp(-\varepsilon). \end{aligned} \tag{2}$$

For simplicity, we consider the lowest order (nonrelativistic) term in this expansion and normalize $f_0 = (2N_0/\sqrt{\pi})\sqrt{\varepsilon}\exp(-\varepsilon)$ by the number of particles N_0 within the initial layer and $f_{\rm inj}$ by the number of particles injected into the layer $N_{\rm inj} \propto V_{\rm in}\tau_{\rm inj}$ during reconnection. With these assumptions, the solution to (1) can be written as

$$\begin{aligned} f(\varepsilon,t) = &\frac{2N_0}{\sqrt{\pi}}\sqrt{\varepsilon}e^{-(3/2+\beta)\alpha t}\exp(-\varepsilon e^{-\alpha t}) \\ &+ \frac{2N_{\rm inj}}{\sqrt{\pi}(\alpha\tau_{\rm inj})\varepsilon^{1+\beta}}[\Gamma_{(3/2+\beta)}(\varepsilon e^{-\alpha t}) - \Gamma_{(3/2+\beta)}(\varepsilon)], \end{aligned} \tag{3}$$

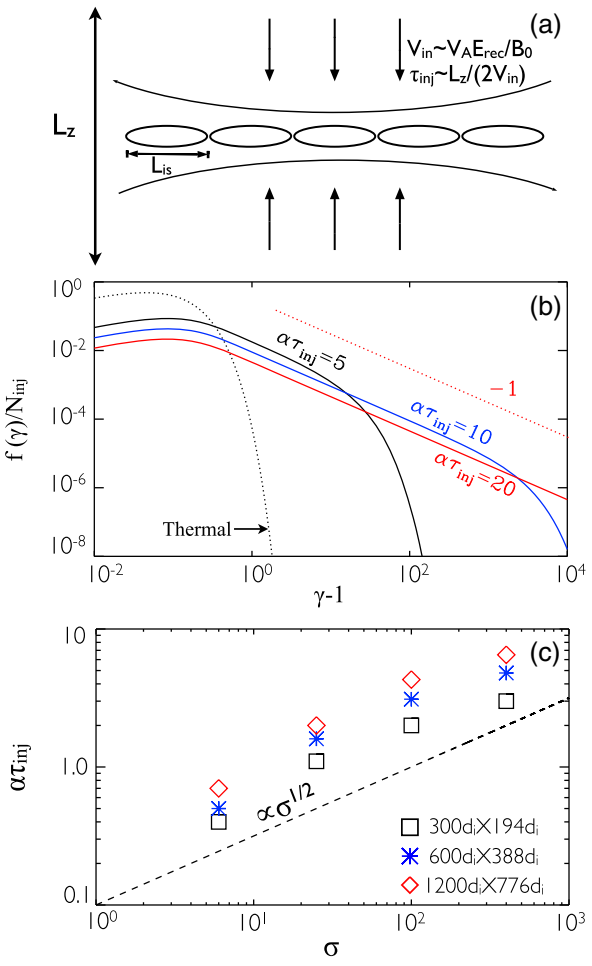

FIG. 3 (color online). (a) Illustration of the acceleration model for the formation of power-law distributions. (b) Analytical results for different $\alpha\tau_{\rm inj}$ obtained from (4). (c) Time integrated $\alpha\tau_{\rm inj}$ for cases with $\sigma = 6$–400 and different system sizes.

where $\beta = 1/(\alpha\tau_{\rm esc})$ and $\Gamma_s(x)$ is the incomplete gamma function. The first term accounts for particles initially in the acceleration region, while the second term describes the evolution of injected particles. In the limit of no injection or escape ($\tau_{\rm esc} \to \infty$ and $\tau_{\rm inj} \to \infty$), the first term in (3) remains a thermal distribution with enhanced temperature $e^{\alpha t}T$, consistent with Ref. [30]. However, as reconnection proceeds, new particles enter continuously into the acceleration region and, because of the periodic boundary conditions, there is no particle escape. Thus, considering the case $\tau_{\rm esc} \to \infty$ and assuming $N_0 \ll N_{\rm inj}$, at the time $t = \tau_{\rm inj}$ when reconnection saturates, the second term in (3) simplifies to

$$f(\varepsilon,\tau_{\rm inj}) = \frac{N_{\rm inj}}{\alpha\tau_{\rm inj}}\left[\frac{\mathrm{erf}(\varepsilon^{1/2}) - \mathrm{erf}(\varepsilon^{1/2}e^{-\alpha\tau_{\rm inj}/2})}{\varepsilon} + \frac{2}{\sqrt{\pi}}\frac{e^{-\alpha\tau_{\rm inj}/2}\exp(-\varepsilon e^{-\alpha\tau_{\rm inj}}) - e^{-\varepsilon}}{\varepsilon^{1/2}}\right]. \quad (4)$$

When $\alpha\tau_{\rm inj} > 1$, this gives the relation $f \propto 1/\varepsilon$ in the energy range $1 < \varepsilon < e^{\alpha\tau_{\rm inj}}$, as shown in Fig. 3(b), by directly evaluating (4) for different $\alpha\tau_{\rm inj}$. Interestingly, this energy range for the power law is below that of the heated thermal particles in the initial layer. Thus, in the limit $N_0 \sim N_{\rm inj}$ the first term in (3) should be retained and the power law produced is subthermal relative to this population. While it is straightforward to obtain the relativistic corrections arising from the injected distribution (2), we emphasize that these terms do not alter the spectral index.

In order to estimate the acceleration rate α, the energy change of each particle can be approximated by a relativistic collision formula (e.g., [32])

$$\Delta\gamma = \left(\Gamma_V^2\left(1 + \frac{2Vv_x}{c^2} + \frac{V^2}{c^2}\right) - 1\right)\gamma, \quad (5)$$

where V is the outflow speed, $\Gamma_V^2 = 1/(1 - V^2/c^2)$, and v_x is the particle velocity in the x direction. The time between two collisions is about $L_{\rm is}/v_x$, where $L_{\rm is}$ is the typical size of the magnetic islands (or flux ropes in 3D). Assuming relativistic particles have a nearly isotropic distribution $v_x \sim c/2$

$$\alpha \sim \frac{c(\Gamma_V^2(1 + \frac{V}{c} + \frac{V^2}{c^2}) - 1)}{2L_{\rm is}}. \quad (6)$$

Using this expression, we measure the averaged V and $L_{\rm is}$ from the simulations and estimate the time-dependent acceleration rate $\alpha(t)$. An example is shown in Fig. 2(c). This agrees reasonably well with that obtained from perpendicular acceleration and curvature drift acceleration. Figure 3(c) shows the time-integrated value of $\alpha\tau_{\rm inj} = \int_0^{\tau_{\rm inj}} \alpha(t)dt$ for various simulations with $\sigma = 6$–400. For cases with $\alpha\tau_{\rm inj} > 1$, a hard power-law distribution with spectral index $p \sim 1$ forms. For higher σ and larger system size, the magnitude of $\alpha\tau_{\rm inj}$ increases approximately as $\propto \sigma^{1/2}$.

Discussion.—Considering the more realistic limit with both particle loss and injection, Eq. (3) predicts a spectral index $p = 1 + 1/(\alpha\tau_{\rm esc})$ when $\alpha\tau_{\rm inj} > 1$, recovering the classical Fermi solution (e.g., [32]). If the escape is caused by convection out of the acceleration region $\tau_{\rm esc} = L_x/V$, the spectral index should approach $p = 1$ when $\alpha\tau_{\rm esc} \gg 1$ in the high-σ regime. Although the present simulations employed periodic boundary conditions, most cases develop power-law distributions within two light-crossing times, indicating that the boundary conditions do not strongly influence the results. In preliminary 2D simulations using open boundary conditions [21], we have confirmed these general trends (Guo *et al.*, 2014, in preparation). For nonrelativistic reconnection, the acceleration rate is lower and thus it takes longer to form a power-law distribution. Take the nonrelativistic limit for (6): if $V = 0.1c$, $v_x = 0.2c$, and $L_{\rm is} = 100d_i$, the reconnection has to be sustained over a time $\tau_{\rm inj} > 2 \times 10^4\omega_{pi}^{-1}$ to form a power law, which significantly exceeds the simulation time of most previous studies. It has been suggested that

current sheet instabilities may strongly influence particle acceleration [13]. In contrast, the energy distributions reported here are remarkably similar in 2D and 3D, despite the broad range of secondary kink and tearing instabilities in 3D. This surprising result suggests that the underlying Fermi acceleration is rather robust and does not depend on the existence of well-defined magnetic islands. The strong similarities between the 2D and 3D acceleration spectra are also consistent with some key similarities in the reconnection dynamics. In particular, the range of scales for the 2D magnetic islands is similar to the observed 3D flux ropes. In addition, the reconnection rate and the flow speeds are also quite similar between 2D and 3D, in agreement with other recent studies [33,34]. In large open systems, it remains to be seen whether 3D turbulence may affect the particle escape times. Another important factor that may influence these results is the presence of an external guide field B_g. Our preliminary simulations suggest that the key results of this letter will hold for $B_g < B_0$. For stronger guide fields, the energy release is slower and the associated particle acceleration requires further study.

We have demonstrated that in the regime $\sigma \gtrsim 1$, magnetic reconnection is an efficient mechanism of converting the energy stored in the magnetic shear into relativistic nonthermal particles. These energetic particles contain a significant fraction of the total energy released and, quite interestingly, have a power-law energy distribution with spectral index $p \sim 1$ when $\alpha\tau_{\rm inj} > 1$. Physically, this requires that the time scale over which particles are injected into the acceleration region is longer than the acceleration time for the first-order Fermi process. The results in this Letter demonstrate this condition is more easily achieved in regimes with $\sigma \gg 1$, but it may also occur with $\sigma \gtrsim 1$ in sufficiently large reconnection layers. Our new findings substantiate the importance of fast magnetic reconnection in strongly magnetized plasmas and may be important in explaining the high-energy emissions in systems like pulsars, jets from black holes, and gamma-ray bursts.

We thank the referees for providing helpful reports for improvement and clarification to the Letter, especially the insightful suggestions regarding the analytical derivation. We gratefully acknowledge our discussions with Andrey Beresnyak and Dmitri Uzdensky. We are grateful for support from the DOE through the LDRD program at LANL and DOE/OFES support to LANL in collaboration with CMSO. This research is part of the Blue Waters sustained-petascale computing project, which is supported by the NSF (Grant No. OCI 07-25070). Additional simulations were performed at the National Center for Computational Sciences at ORNL and with LANL institutional computing.

[1] M. Hoshino and Y. Lyubarsky, Space Sci. Rev. **173**, 521 (2012).
[2] J. G. Kirk, Phys. Rev. Lett. **92**, 181101 (2004).
[3] D. Giannios, Mon. Not. R. Astron. Soc. **408**, L46 (2010).
[4] C. Thompson, Mon. Not. R. Astron. Soc. **270**, 480 (1994).
[5] B. Zhang and H. Yan, Astrophys. J. **726**, 90 (2011).
[6] J. Arons, Space Sci. Rev. **173**, 341 (2012).
[7] P. L. Pritchett, J. Geophys. Res. **111**, A10212 (2006).
[8] X. R. Fu, Q. M. Lu, and S. Wang, Phys. Plasmas **13**, 012309 (2006).
[9] M. Oka, T.-D. Phan, S. Krucker, M. Fujimoto, and I. Shinohara, Astrophys. J. **714**, 915 (2010).
[10] E. M. de Gouveia dal Pino and A. Lazarian, Astron. Astrophys. **441**, 845 (2005).
[11] J. F. Drake, M. Swisdak, H. Che, and M. A. Shay, Nature (London) **443**, 553 (2006).
[12] S. Zenitani and M. Hoshino, Astrophys. J. **562**, L63 (2001).
[13] S. Zenitani and M. Hoshino, Astrophys. J. **670**, 702 (2007).
[14] B. Cerutti, G. R. Werner, D. A. Uzdensky, and M. C. Begelman, Astrophys. J. **770**, 147 (2013).
[15] L. Sironi and A. Spitkovsky, Astrophys. J. **783**, L21 (2014).
[16] W. Liu, H. Li, L. Yin, B. J. Albright, K. J. Bowers, and E. P. Liang, Phys. Plasmas **18**, 052105 (2011).
[17] N. Bessho and A. Bhattacharjee, Astrophys. J. **750**, 129 (2012).
[18] V. S. Titov, K. Galsgaard, and T. Neukirch, Astrophys. J. **582**, 1172 (2003).
[19] K. Galsgaard, V. S. Titov, and T. Neukirch, Astrophys. J. **595**, 506 (2003).
[20] K. J. Bowers, B. J. Albright, L. Yin, W. Daughton, V. Roytershteyn, B. Bergen, and T. J. T. Kwan, J. Phys. Conf. Ser. **180**, 012055 (2009).
[21] W. Daughton, J. Scudder, and H. Karimabadi, Phys. Plasmas **13**, 072101 (2006).
[22] W. Daughton and H. Karimabadi, Phys. Plasmas **14**, 072303 (2007).
[23] W. Daughton, Phys. Plasmas **6**, 1329 (1999).
[24] L. Yin, W. Daughton, H. Karimabadi, B. Albright, K. Bowers, and J. Margulies, Phys. Rev. Lett. **101**, 125001 (2008).
[25] E. G. Blackman and G. B. Field, Phys. Rev. Lett. **72**, 494 (1994).
[26] M. Lyutikov and D. Uzdensky, Astrophys. J. **589**, 893 (2003).
[27] Y. E. Lyubarsky, Mon. Not. R. Astron. Soc. **358**, 113 (2005).
[28] S. Zenitani, M. Hesse, and A. Klimas, Astrophys. J. **696**, 1385 (2009).
[29] M. Melzani, R. Walder, D. Folini, C. Winisdoerffer, and J. M. Favre, arXiv:1404.7366.
[30] J. F. Drake, M. Opher, M. Swisdak, and J. N. Chamoun, Astrophys. J. **709**, 963 (2010).
[31] J. T. Dahlin, J. F. Drake, and M. Swisdak, Phys. Plasmas **21**, 092304 (2014).
[32] M. S. Longair, *High Energy Astrophysics: Vol. 2, Stars, the Galaxy and the Interstellar Medium*, 2nd ed. (Cambridge University, Cambridge, England, 1994).
[33] Y.-H. Liu, W. Daughton, H. Karimabadi, H. Li, and V. Roytershteyn, Phys. Rev. Lett. **110**, 265004 (2013).
[34] W. Daughton, T. K. M. Nakamura, H. Karimabadi, V. Roytershteyn, and B. Loring, Phys. Plasmas **21**, 052307 (2014).